Monitoring tissue implants by field-cycling 1H-MRI via the detection of changes in the 14N-quadrupolar-peak from imidazole moieties incorporated in a "smart" scaffold material

UNIVERSITÀ DEGLI STUDI DI TORINO

Monitoring tissue implants by field-cycling ^{1}H-MRI via the detection of changes in the ^{14}N-quadrupolar-peak from Imidazole moieties incorporated in a "smart" scaffold material

Enza Di Gregorio[†a], Valeria Bitonto[†a], Simona Baroni[a], Rachele Stefania[a], Silvio Aime[a], Lionel M. Broche[b], Nicholas Senn[b], P. James Ross[b], David J. Lurie[b], Simonetta Geninatti Crich[a].*

[a] Department of Molecular Biotechnology and Health Sciences, University of Torino, via Nizza 52, Torino, Italy

[b]Aberdeen Biomedical Imaging Centre, University of Aberdeen, Foresterhill, AB25 2ZD, Aberdeen, U.K.

Corresponding Author: Simonetta Geninatti Crich

E-Mail: simonetta.geninatti@unito.it

† These authors contributed equally to this work.

Keywords: *biomaterial for tissue engineering, fast field-cycling magnetic resonance imaging (FFC-MRI), quadrupole peaks, imaging probes, regenerative medicine*

Abstract

This study is focused on the development of innovative sensors to non-invasively monitor the tissue implant status by Fast-Field-Cycling Magnetic Resonance Imaging (FFC-MRI). These sensors are based on oligo-histidine moieties that are conjugated to PLGA polymers representing the structural matrix for cells hosting scaffolds. The presence of ^{14}N atoms of histidine causes a quadrupolar relaxation enhancement (also called Quadrupolar Peak, QP) at 1.39 MHz. This QP falls at a frequency well distinct from the QPs generated by endogenous semisolid proteins. The relaxation enhancement is pH dependent in the range 6.5-7.5, thus it acts as a reporter of the scaffold integrity as it progressively degrades upon lowering the microenvironmental pH. The ability of this new sensors to generate contrast in an image obtained at 1.39 MHz on a FFC-MRI scanner is assessed. A good biocompatibility of the histidine-containing scaffolds is observed after its surgical implantation in healthy mice. Over time the scaffold is colonized by endogenous fibroblasts and this process is accompanied by a progressive decrease of the intensity of the relaxation peak. In respect to the clinically used contrast agents this material has the advantage of generating contrast without the use of potentially toxic paramagnetic metal ions.

1. Introduction

Nowadays, one of the most important challenges in many medical fields is represented by the application of regenerative medicine approaches, *i.e.* the possibility to repair and/or replace tissues and organs that have been damaged by disease, trauma or congenital defects. [1–3] Different biomaterials have been considered to offer suitable microenvironments for enhancing cell engraftment, including both naturally occurring and synthetic polymers, ceramics, metals and composites [4,5] that act as a temporary support for cell proliferation and tissue regeneration.[6] However, routine use in clinical applications has been hampered due to rapid scaffold degradation and poor long-term survival of therapeutic cells.[7] In particular, it is not well understood whether graft failure is the consequence of cell death and when this occurs. On this basis, a non-invasive imaging method that can probe implant status and cell viability would accelerate the clinical translation of these approaches. To date there are no methods that can monitor the scaffold status *in vivo* and report on its degradation and on the vitality of the transplanted or colonizing cells. Most of the explored methods involve the use of fluorescent probes added to the implant whose detection is readily possible *in vitro* before implantation but hampered, if not impossible, at the patient level. [8] In fact, whereas light tissue penetration allows the use of optical imaging in small animals [9,10], the only way to monitor artificial tissue over time in humans is to resort to the surgical removal of a tissue sample to be analyzed *ex vivo*. MRI is a powerful high resolution technique capable of providing extremely detailed morphological images. [11] By using Gd-based contrast agents (GBCAs) or highly sensitive iron oxide particles, it is possible to label various types of cells or implants making them detectable by means of MRI. [12–16] Major disadvantages, however, arise from the cytotoxicity of the metals used and the persistence of the contrast in the image even after implant degradation and cell death have occurred. For these reasons, probe developers are challenged to find

alternative metal-free solutions, with special attention to solutions that could allow for long-term *in vivo* monitoring applications. In this context, one example consists of MRI detectable CEST (Chemical Exchange Saturation Transfer) agents based on hydrogels, recently proposed for *in vivo* detection of transplanted cell viability.[17,18] The contrast is generated by the pH-dependent saturation transfer caused by arginine exchangeable protons loaded into a liposome cavity. However, the diamagnetic CEST agents showed a lower sensitivity with respect to the paramagnetic ones, also because of the strong background of endogenous exchangeable protons whose resonances fall in the same range of arginine signals (e.g. polypeptide amide and amine groups, etc…).

In this study, an innovative biocompatible, biodegradable and trackable material was developed for the preparation of tissue implants. The peculiarity of this material is that it contains an intrinsic sensor able to self-generate T_1 contrast in an MR image without the addition of paramagnetic metals. The biomaterial consists of PLGA (Poly-Lactic and Glycolic Acid) already approved for human use, forming the solid matrix of the scaffold. [19,20] The sensing component of the biomaterial consists of histidine oligomers (oligo-His) able to generate a relaxation enhancement at a specific frequency well detectable by Fast Field-Cycling Magnetic Resonance Imaging (FFC-MRI).[21,22] The relaxometric response of this material can be followed over the entire lifetime of the scaffold. The uniqueness of the FFC-MRI technology relies on its ability to yield images based on how the magnetic relaxation time of water protons varies with the applied magnetic field strength, i.e. by providing the Nuclear Magnetic Relaxation Dispersion (NMRD) profile of any material able to affect the proton relaxation rates. FFC is the only practical way of measuring NMRD profiles *in vivo* and producing images at variable and low magnetic field strengths in a relatively short time, compatible with the clinical practice. It involves switching the magnetic field between different field strengths during the measurement procedure. The time to switch between levels has to be less than the sample relaxation time, in which case the technique is known as “fast” field-cycling (FFC). FFC-NMR

relaxometry has been widely exploited in recent years worldwide on small solid and liquid samples [23,24] and, recently, also *in vivo* on solid tumors implanted in the mouse hind limb.[25,26] However, FFC has only recently been applied to MRI, and two prototype human whole-body sized FFC-MRI scanners have been built at the University of Aberdeen.[21,22] FFC-MRI/NMR has the advantage to allow the detection of the frequency-dependent relaxation enhancement described as the Quadrupolar Peaks (QPs) contribution[27,28] and this ability is further exploited in the herein reported work. QPs result from local increases in the NMRD profile at magnetic fields where the proton NMR frequency and the ^{14}N nuclear quadrupole resonance frequency coincide; it possesses simultaneously the high signal-to-noise ratio of proton imaging while reporting on the effects associated with the presence of ^{14}N nuclei. [29–32] Certain well-defined QP signals are naturally present in many biological tissues.[33] They are generated by water interaction with ^{14}N atoms present in the protein amidic groups. Biological tissues display three QPs due to the amide functionalities of endogenous, immobilized proteins (0.7, 2.1 and 2.8 MHz). However, the sensor proposed here is based on ^{14}N-containing compounds that are able to generate QPs clearly distinguishable from the previously known ones. We recently reported [34] that exogenous poly-Histidine (poly-His) containing systems of different sizes show a further QP in addition to the endogenous ones, thus paving the way for the development of a totally new class of metal-free ^{1}H-MRI frequency-encoded specific reporters. The contrast is derived from imidazole groups of oligo-histidine chains causing Quadrupolar Relaxation Enhancement (QRE) at 1.39 MHz, readily detectable by an FFC-MRI scanner. The immobilization of the polymeric chains in a tissue-like state is mandatory for the generation of the QRE.[31] Thus QRE can be exploited for monitoring scaffold water permeation and consequently the scaffold surface or bulk erosion. Since pH controls the physical state of the oligo-His solid/liquid status, an estimate of the pH of the microenvironment in which the sensor is located can be obtained via the changes in the QRE intensity thus providing at the same time valuable information on cell viability and graft degradation. An

increase in oligo-His mobility due to the pH decrease associated with cell proliferation[35] may also be detected when the imidazole units are still part of a scaffold matrix, thus acting as reporters of local physiological and pathological changes. Accordingly, the conjugation of an oligo-His chain to the polymeric biomaterial can allow the physician to assess, in real time, the status of the transplanted scaffold and cells, monitoring the natural biodegradation of the scaffold and the cells' colonization. The idea of developing MRI contrast agents based on the generation of a QRE has also been recently reported.[36–38] The study investigated ^{209}Bi (I=9/2) containing organometallic compounds reporting interesting results at magnetic field strengths near to the clinical ones. However, the translation to human studies appeared difficult due to the Bi toxicity and low water solubility of these compounds.

2. Material and Methods

2.1 Chemicals: Resomer® RG 502 H (Poly-(D,L-lactide-co-glycolide, 50:50, acid terminated, Mw 7,000-17,000), Resomer® RG 504 H (Poly-(D,L-lactide-co-glycolide, 50:50, acid terminated, MW 38000-54000), Sucrose, Tetraglycol, Poly-(vinyl alcohol) (PVA, MW 31000-50000), diaminobenzidine enhanced liquid substrate chromogen system (D3939) and all other chemicals were purchased from Sigma-Aldrich Co. LLC. Anti-rabbit CD68 (ab125212) and goat anti-rabbit (ab97051) were purchased from Abcam.

2.2 Scaffold fabrication: Different polymer formulations were considered in this study, namely: *i)* commercially available not functionalized PLGA polymers of different size (Resomer® RG 502 H (7-17 kDa) hereinafter labeled as Small (S) or Resomer® RG 504 H (38-54 kDa) herein after labeled as Large (L)) and *ii)* the correspondent derivatives conjugated with the oligo-His peptide synthetized in our laboratory (oligo-His-PLGA-S and oligo-His-PLGA-L). PLGA scaffolds were prepared by dissolving PLGA in tetraglycol at 200 mg ml^{-1} by stirring overnight

at 60 °C. In order to create porous scaffold for *in vivo* implant, 300 μL of 75(L):25(S) PLGA or oligo-His-PLGA were placed in a cylindrical mold equipped with a piston and mixed with 180 mg of sucrose. The polymer solution was then injected into 30 mL of phosphate buffer (PBS) containing 0.3% w/w of PVA, where it precipitated by phase inversion to form a solid scaffold as tetraglycol diffused into PBS and allowed the porogen to be leached from the scaffold to form a porous structure. The scaffolds were placed at 4°C O/N, before being washed three times in PBS and sterilized in 70% ethanol solution for 10 minutes.

2.3 Animals and in vivo scaffold implant: Balb/c mice (Charles River Laboratories, Calco, Italy), bred at the animal house of the Molecular Biotechnology Center of the University of Torino, were used for the *in vivo* experiments (n = 12 for each group, mean weight 22 ± 1 g). Mice were kept in standard housing with standard rodent chow and water available ad libitum, and a 12 h light/dark cycle. Experiments were performed according to national rules and policies on animal handling and authorized by the Italian Ministry of Health (authorization number 807/2017PR). Before the scaffold implantation, mice were anaesthetized by intramuscular injection of tiletamine/zolazepam (Zoletil 100; Virbac, Milan, Italy) 20 mg kg^{-1} plus xylazine (Rompun; Bayer, Milan, Italy) at the dose of 5 mg kg^{-1}. After scrubbing with betadine, a 15 mm dorsal midline incision was made over the thoracolumbar area. The PLGA or oligo-His-PLGA scaffold was subcutaneously inserted and then the wound sutured. Scaffold was monitored twice a week with MRI. After 12 and 25 days from implant mice were euthanized. Scaffold implants were collected for NMRD acquisition and subsequent histological evaluations.

2.4 MRI acquisition: MR images of implanted scaffold in mice were acquired at 7.1 T on a Bruker Avance Neo 300 MHz spectrometer equipped with the Micro 2.5 microimaging probe at room temperature (R.T. = 21 °C). T_{2W} images were acquired by using a standard RARE

(Rapid Acquisition with Refocused Echoes) sequence with the following parameters: TR = 4000 ms, TE = 24 ms, RARE factor = 16, flip angle = 180°, number of averages = 4, FOV = 28 mm × 28 mm, slice thickness = 1 mm, matrix size 256 × 256.

T_2 values were measured using a MSME (multislice multiEcho) sequence (TR = 3500 ms, 200 variable TE ranging from 3 to 600 ms, FOV = 1 x 1 cm, slice thickness = 1 mm, matrix size 128 x 128). A glass tube containing a 0.5 mM ProHance solution (Bracco Imaging, Milan, Italy) as reference was inserted close to the mouse body.

2.5 FFC imaging acquisition: FFC images were acquired using a whole-body FFC-MRI scanner [21] with a custom-made radiofrequency coil (5-turns of 2 mm gauge enamelled copper wire, 3.5 cm diameter, 3 cm high, Q factor of 189 at 8.65 MHz) at room temperature. T_1 images were acquired using a field-cycling inversion recovery sequence[39] across 12 evolution times logarithmically spaced between 200 and 4000 ms, evolution magnetic field strengths of 25, 33, 38 and 63 mT, matrix size of 32 × 32, FOV of 72 mm, slice thickness of 30 mm, and echo time of 16 ms, 10 kHz bandwidth, 800 μs gradient ramp time, 1 ms crusher gradient and 20 ms B_0 ramp time, with total scan duration of approximately 90 min. NMR dispersion (NMRD) profiles were obtained from a surface fit of the averaged signal obtained from regions-of-interest of 2-by-2 voxel area. The percentage increase of R_1 at sensor field of 33 mT relative to the baseline field of 38 mT was determined.

2.6 NMRD profile acquisition: NMRD profiles, i.e. Proton longitudinal relaxation time (T_1) values as a function of the magnetic field strength (from 0.01 to 10 MHz Proton Larmor Frequencies), were acquired at 25°C on a SPINMASTER FFC2000 NMR relaxometer (Stelar S.n.c., Mede (PV), Italy) equipped with a 10 mm 0.5 T FC magnet and microcoil. Scaffolds were placed in a capped glass micro-tube (5 mm diameter x 10 mm length). The temperature was controlled by a Stelar VTC-91 airflow heater, equipped with a copper-constantan

thermocouple. The temperature in the probe head was measured with a Fluke 52 k/j digital thermometer (Bassersdorf, Switzerland). The relaxometer operated under complete computer control with an absolute uncertainty in the $1/T_1$ values of ±2%. T_1 measurements were performed by using the Not Polarized and Pre-Polarized sequences as described by Ferrante and coworkers [40] with 16 values of delay time (τ).

2.7 *Histological studies:* After NMRD acquisition scaffolds were placed overnight in buffered 4% formaldehyde solution and then included in paraffin. Dewaxed 5 μm sections were stained with haematoxylin-eosin and chloroacetate esterase staining. For immunohistochemistry assays, de-waxed 5 mm sections were submitted to wet heat-induced antigen retrieval in a mixture of 0.1 M Tris and 0.01 M EDTA solution at pH 9.0. Endogenous peroxidase was blocked in 0.6% hydrogen peroxide solution in 0.05 M TBS (pH 7.6) for 20 minutes at room temperature. Sections were then treated with 5% normal goat serum and reacted overnight with goat anti-rabbit CD68. Subsequently, sections were incubated with goat anti-rabbit IgG conjugated to HRP for 1 hour at room temperature. Finally, sections were treated with diaminobenzidine enhanced liquid substrate chromogen system and counterstained with hematoxylin.

2.8 Statistical analysis. Data are represented as mean ±SD. Statistical significance of results was evaluated by using an unpaired two-tails Student's t-test. Results were considered significant at 99% (**) if $P < 0.01$.

3. Results and Discussion

3.1. Synthesis of oligo-His peptide and conjugation with PLGA

We have recently reported the fast and easy synthesis of PLGA-oligo-His via a thiol-Michael addition reaction between PLGA-PEG_2-Maleimide and oligo-His containing a N-terminal cysteine residue (aminoacid sequence: $CGGH_n\beta A$, n=15).[34] The oligo-His peptide was synthesized by standard 9-fluorenylmethyloxycarbonyl solid-phase peptide synthesis (Fmoc-SPPS) carried out on a Liberty CEM microwave synthesizer. Herein (Figure 1), we prepared two maleimide functionalized PLGA namely PLGA-PEG_2-Mal-S and PLGA-PEG_2-Mal-L starting from Resomer® RG 502 H (MW= 12800 Da) and Resomer® RG 504 H (MW=52900 Da), respectively, by coupling their carboxyl group with the amino group of the Maleimide-PEG_2-NH_2. Next, in order to get oligo-His-PLGA-S and oligo-His-PLGA-L, PLGA-PEG_2-Mal-S and -L were covalently linked with $CGGH_{15}\beta A$ (for synthesis details see Supporting Information). The products were analyzed by ^{1}H-NMR-spectroscopy (600 MHz, dmso-d6, **Figure S1** and **Figure S2**).

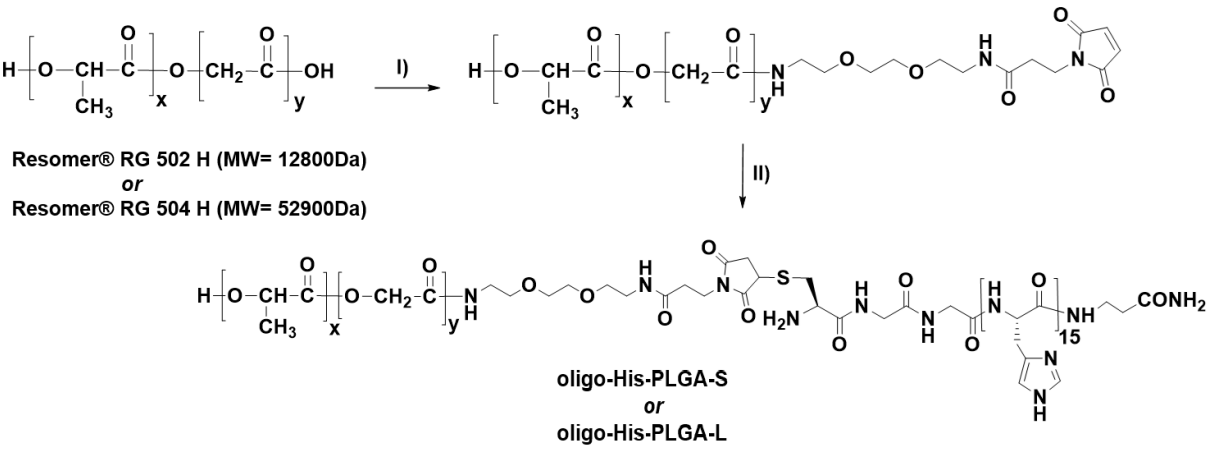

Figure 1. Schematic synthesis of oligo-His-PLGA-S and oligo-His-PLGA-L: I) (1-[Bis (dimethylamino)methylene]-1H-1,2,3-triazolo[4,5-b]pyridinium3-oxid hexafluorophosphate (HATU), diisopropylethylamine (DIPEA), Maleimide-PEG_2-NH_2 in acetonitrile (CH_3CN); II) $CGGH_{15}\beta A$ (oligoHis), DIPEA in N, N-dimethylformamide (DMF).

3.2. Oligo-His-PLGA and PLGA scaffold preparation

Porous oligo-His-PLGA- and PLGA-based scaffolds were prepared by applying the porogen leaching technique. [41] The oligo-His-PLGA or PLGA were dissolved in tetraglycol (200 mg ml^{-1}). The solution was placed in a syringe together with the porogen (glucose, 600 mg ml^{-1}). It was then injected into a poly-vinyl alcohol (PVA, 0.3% w/w) solution in PBS, where it precipitated by phase inversion to form a solid scaffold. Water slowly diffuses into the PLGA solid scaffold allowing the porogen to be leached, thus forming a porous structure. The scaffold was washed three times to eliminate the PVA excess. The formulation yielding a material endowed with sufficient consistency and high QRE was achieved using the 75:25 ratio of oligo-His-PLGA-L and oligo-His-PLGA-S, respectively. This formulation was selected after several attempts, as reported in **Table S1** of Supplemental Materials. From the data analysis, it was possible to conclude that the use of PLGA with a molecular weight around 50 kDa is necessary to obtain a good precipitation when passing from tetraglycol to aqueous solution. On the other hand, it is necessary to take into account that the longer the polymer chain, the smaller percentage of His is found in the final product for the same weight of material.

The Nuclear Magnetic Relaxation Dispersion (NMRD) profile acquired on this biomaterial showed several peaks due the presence of ^{14}N centres in different chemical environments (two on the imidazole moieties and one on the amide groups of the polypeptide chains). However, the most prominent one that appears, well distinct from the amide-corresponding ones, is the peak at 1.39 MHz associated with the presence of the imidazole groups.

The QRE was calculated using the following equation:

$$QRE = (R_1^{1.39\,MHz} - R_1^{1.68\,MHz})/R_1^{1.68\,MHz} * 100$$
$$= \Delta R_1/R_1^{1.68\,MHz} * 100 \quad (1)$$

Where R_1 is the proton longitudinal relaxation rate measured at the indicated proton Larmor frequency.

Figure 2A shows that the QRE of oligo-His-PLGA was ca. 40 %, corresponding to a ΔR_1 of ~1.1 s^{-1}. The protonation of the imidazole group of the histidine (pK_a=6.8)[42,43] increases its solubility in water with a consequent increase in mobility and progressive disappearance of the QPs at pH < 6.5. **Figure 2B** shows the pH dependence of ΔR_1 (at 1.39 MHz) which results in the ability to monitor changes in the implant status.

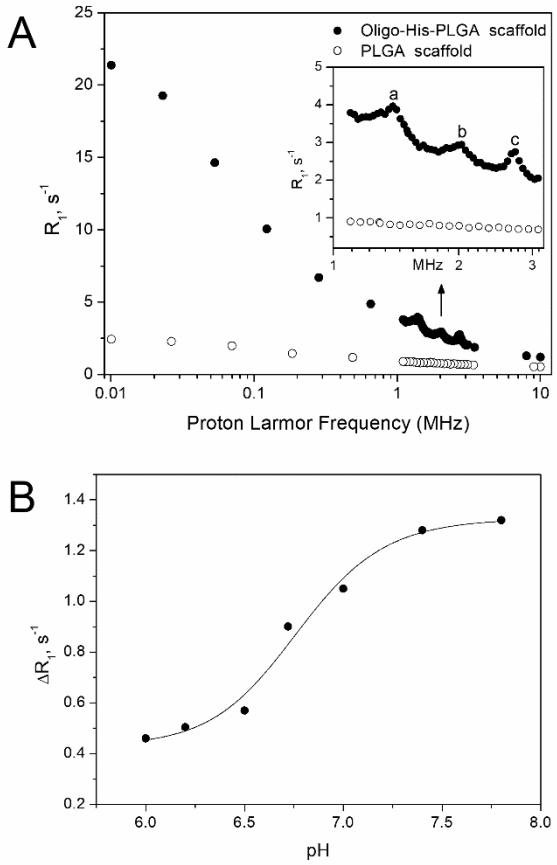

Figure 2. (A) NMRD profiles of Oligo-His-PLGA (●) and PLGA scaffolds (○); the inset shows the magnification of the three QPs, arising from the imidazole group (a, 1.39MHz) and from the amide groups of the oligopeptide (b, 2.1 and c, 2.7 MHz) respectively; (B) ΔR_1 (s^{-1}) of oligo-His-PLGA scaffolds measured at 1.39 MHz as a function of the pH.

3.3. FFC-MRI

The contrast-generating ability of oligo-His-PLGA scaffold was assessed using the 0.2 T FFC imager built at the University of Aberdeen. [21] Two oligo-His samples at pH 6.4 and 7.4,

respectively, and a control containing an empty PLGA scaffold were prepared in 10 mm diameter plastic vials and placed in a larger 2% agarose gel phantom with a diameter of 50 mm (see **Figure S3**). FFC images were obtained at four different magnetic field strengths: 25, 33, 38 and 63 mT. For each field strength, separate images were obtained at 12 logarithmically spaced evolution times, spaced between 200 ms and 4000 ms. From this image set NMRD profiles were derived by fitting the signal intensity to an exponential model (**Figure S4**). All FFC-MRI images were obtained using a field-cycling inversion recovery sequence with a spin-echo readout (TE = 16 ms, number of averages = 1, FOV = 72 mm, slice thickness = 30 mm, matrix size = 32x32).

QP contrast images of the scaffold samples included in 2 % Agarose gel were obtained at 33 mT (corresponding to the proton Larmor frequency of 1.39 MHz), by subtracting the estimated baseline of the NMRD profile on a voxel-by-voxel basis. Scaffolds containing oligo-His showed a distinctive positive image contrast originating from the oligo-His quadrupolar-induced relaxation differences at 33 mT (Figure 4) The pH 7.4 scaffold yielded 3.8 times higher QP amplitude than the scaffold at pH 6.4 (**Figure 3**).

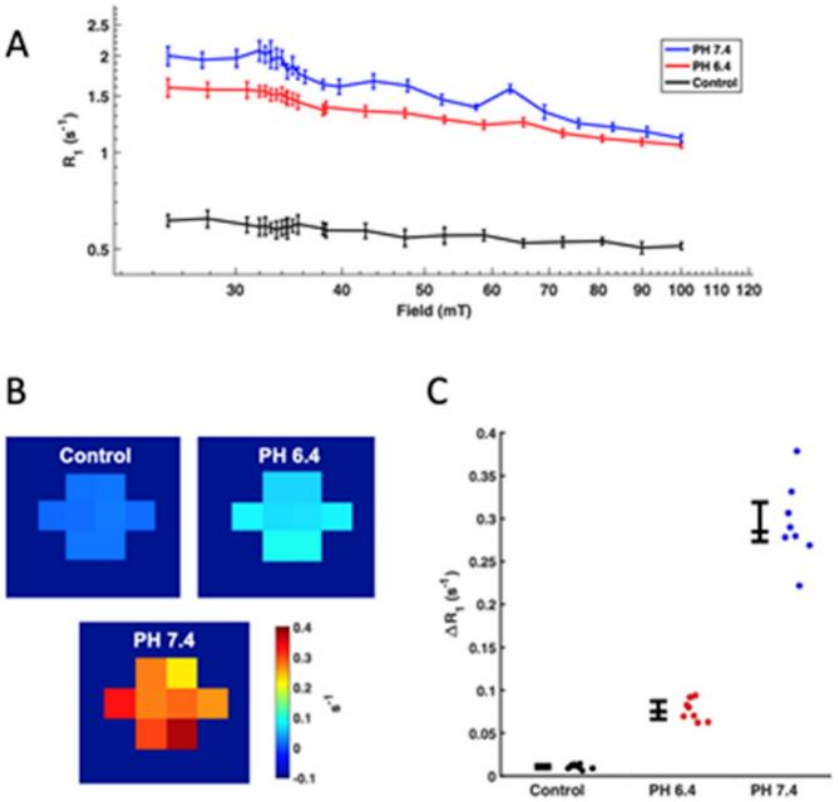

Figure 3 . (A) NMRD profiles of the Oligo-His-PLGA (pH=6.4 and 7.4) and PLGA (control sample) scaffolds, where error bars represent the 95% confidence interval. (B) QP contrast image measured at 33 mT where the image voxel size is 2.25 × 2.25 × 30 mm^3. (C) Dot plot of QP magnitude for each scaffold sample. Each dot represents a single image voxel. The median and IQR is indicated for each sample.

3.4. Scaffolds implantation

Oligo-His-PLGA and PLGA (control) scaffolds were surgically implanted in the upper part of the back of Balb/c mice as shown in **Figure S5**.

After surgery, mice underwent MRI (7 T) examination every four days from day one (t=1) up to 25 days (t=25) from the implantation. T_2-weighted MR images showed that scaffolds are stably encapsulated in the subcutaneous region. **Figure 4** and **Figure S6** show a significant scaffold volume reduction over time, due to the occurrence of surface and bulk degradation of the scaffolds. During the first week, the volume reduction was faster likely with a determinant contribution of the collapse of the larger air-containing pores. Once the situation stabilized (after the first week), the degradation process became slower for both PLGA and oligo-His-

PLGA scaffolds (Figure S4). Mice (n=12 for each sample group) were euthanized 12 and 25 days after surgery; the scaffolds were explanted and analyzed by means of FFC-NMR and histology. MRI revealed a significant decrease of the transverse relaxation time (T_2) for oligo-His-PLGA scaffolds during the time after implantation (from T_2= 55±11 ms to 21±1 at t=1 and t=25, respectively) (**Table S2**). Conversely, for unfunctionalized PLGA scaffold, T_2 remained constant until day 19 and then increased from 88±3 ms to 143 ± 4 at t=19 and t=25, respectively. The different behaviours observed for functionalized oligo-His-PLGA with respect to un-functionalized one, may be accounted for by the different percentage of host cells colonizing the two scaffolds as assessed by histological analysis of the excised scaffolds (see below). The oligo-his-PLGA scaffold showed a higher and faster cell colonization that may be responsible for the observed T_2 decrease.

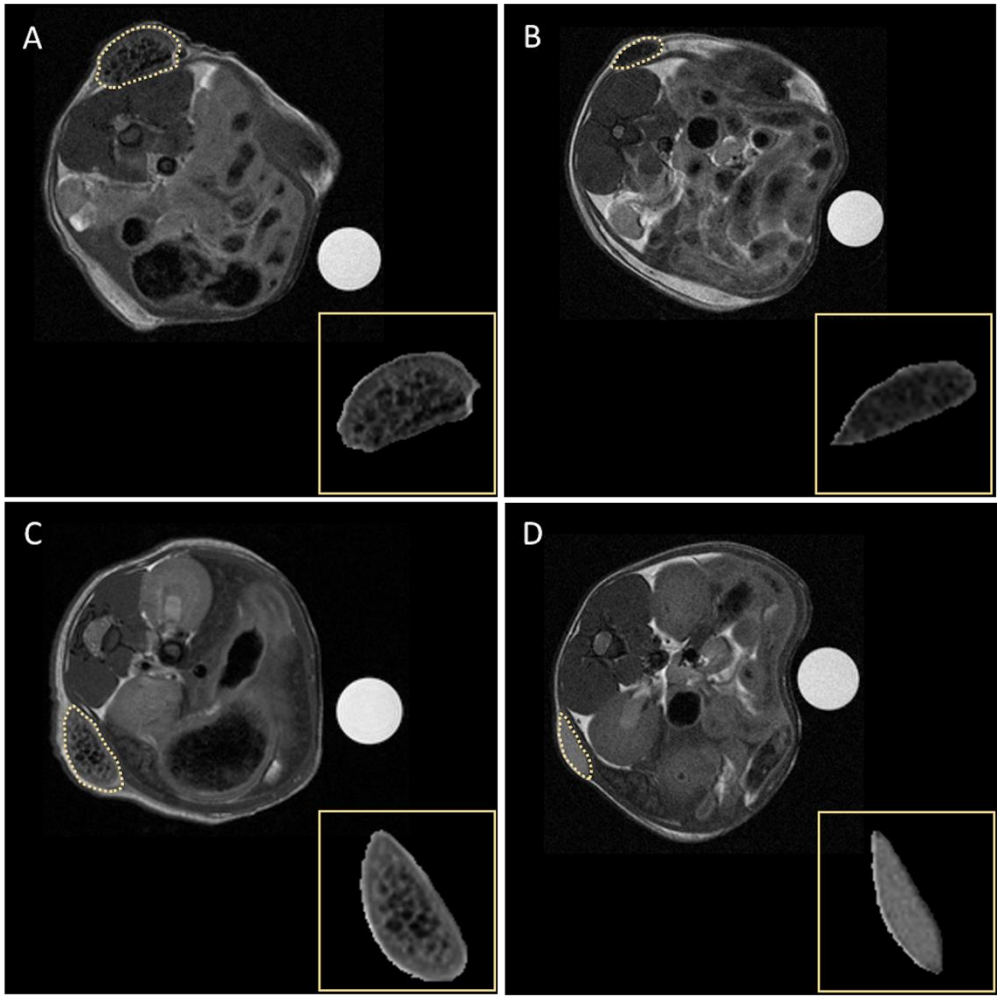

Figure 4. T_{2w}-MRI acquisitions of oligo-His-PLGA- (A, B) and PLGA- (C, D) scaffolds one day after implantation (A, C) and after 25 days (B, D).

Figure 5 shows that, as expected, QPs were clearly detectable at 1.39, 2.03 and 2.7 MHz only on oligo-His-PLGA scaffolds, while PLGA control profiles, in this region, remained flat. All scaffolds showed a significant increase of the overall relaxation profile and QRE after implantation with respect to pre-implant measurements (Figure 5A). This appears to be the consequence of *i)* the replacement of air by water molecules characterized by a restricted mobility inside the pores; *ii)* the extent of the cellular colonization and *iii)* the overall increased compactness of the implant materials. Scaffolds analyzed 25 days after implant showed reduced QREs with respect to 12 days as a consequence of the gradual substitution of scaffold matrix with newly *in situ* generated tissue (Figure 5B, C). This process was monitored by the QRE quantification using Equation 1 (more specifically, ΔR_1 were calculated by considering the differences between the R_1 values measured at the following proton Larmor frequency values: 1.39 and 1.68 MHz, 2.03 and 4.4 MHz, 2.73 and 3.1 MHz, respectively). Figure 5D shows, 25 days after surgery, a QRE decrease at 1.39 MHz of ca. 18 %, probably due to pH change after cells' colonization. Matrix substitution with the regenerated tissue was further demonstrated by the observation of a less pronounced QRE decrease at 2.03 and 2.7 MHz (5.3 and 12% respectively) due to the contributions arising from proteins of the newly generated tissue that fall at these frequencies. These findings outline once again the potential of the FFC-NMR/MRI technique's ability to report on changes in relaxation of materials at different magnetic field strength, to provide unique information, not detectable on scanners operating at a single frequency.

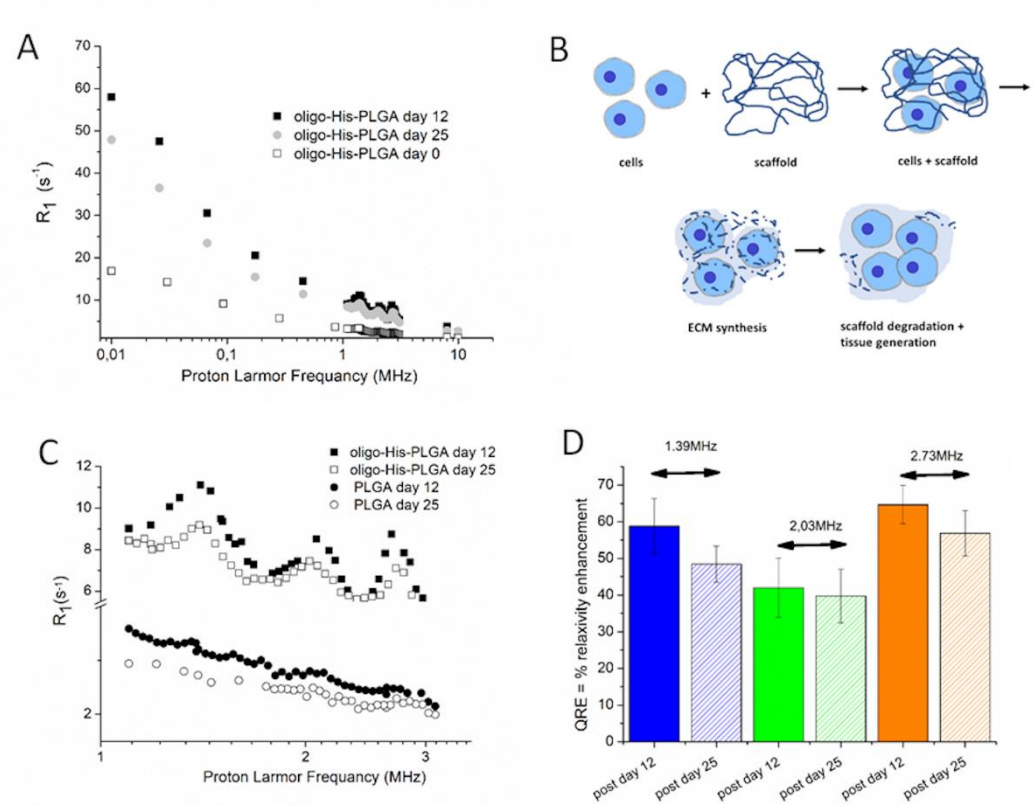

Figure 5. (A) NMRD profiles (0.01-10 MHz, 25°C) of oligo-His-PLGA scaffolds acquired *ex vivo* before and 12 and 25 days after surgical implantation; (B) Representation of scaffold degradation and cell colonization; (C) NMRD profiles (1-3.5 MHz, 25°C) of oligo-His-PLGA and PLGA scaffolds acquired *ex vivo* 12 and 25 days after surgical implantation. (D) % QRE analysis (error bars indicate standard deviation, day 12 n=6, day 25 n=6).

3.5. Histological analysis

Histological analysis of the explanted materials revealed a progressive colonization by mouse endogenous cells, starting from the periphery and moving toward the centre of the scaffolds. After 12 days from *in vivo* implant, Haematoxylin and Eosin (H&E) staining clearly showed an initial cell invasion of the structures, with endogenous cells surrounding all the external surface of the scaffold. After 25 days, cells colonize the entire scaffolds pores and the exogeneous materials start to degrade (**Figure 6**). The H&E quantitative analysis (**Figure 7**) confirmed this observation, showing a correlation between the percentage of the haematoxylin positive area (corresponding to cells invading the scaffold) and days after scaffold implant. The high

collagen deposition observed on scaffold sections, stained with the Masson Trichrome assay (**Figure S7**), demonstrated that most of the colonising cells were fibroblasts.

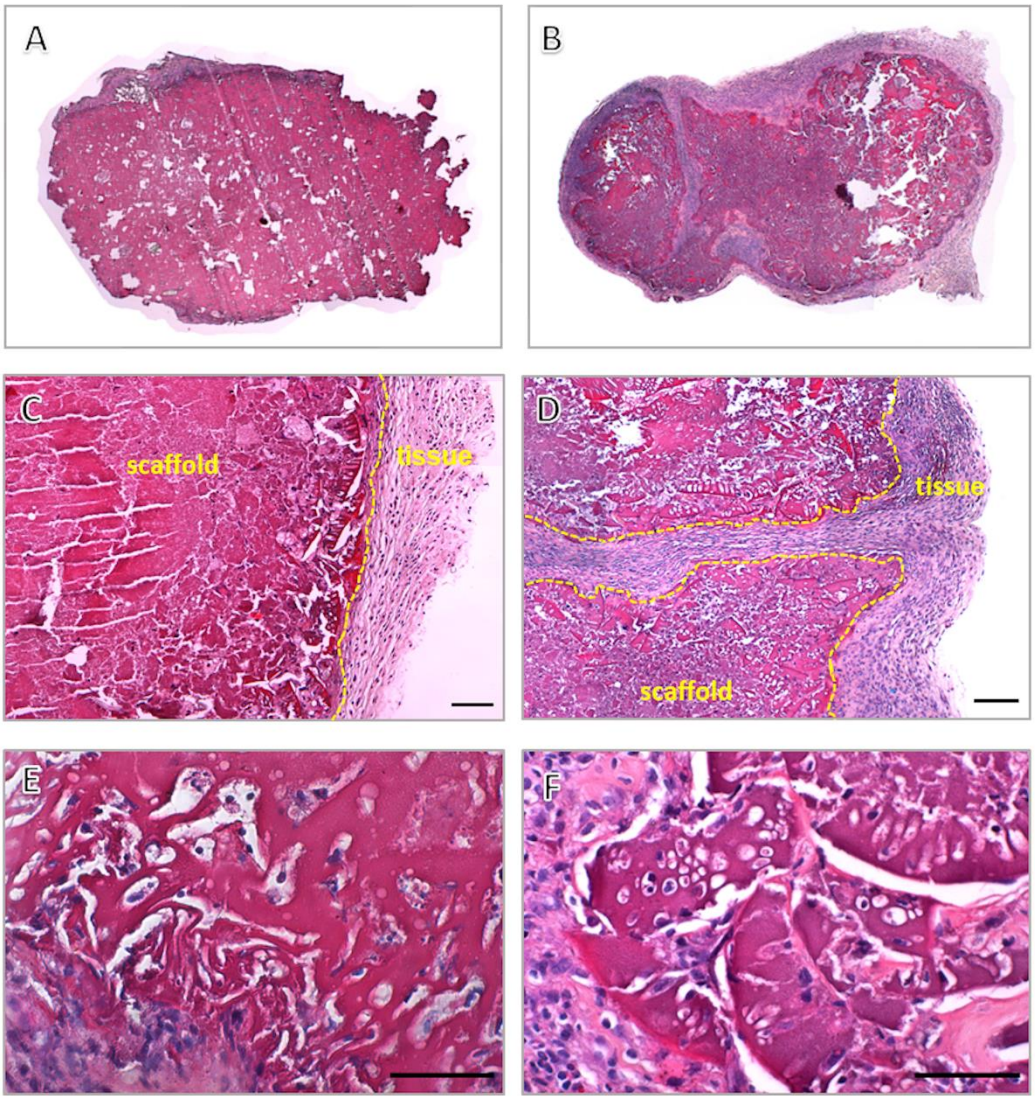

Figure 6. H&E images of oligo-His-scaffolds explanted after 12 days (A) and 25 days (B) were reconstructed from multiple pictures (magnification × 2.5); (C-D) H&E images showing gradual scaffold colonization and invasion by mouse endogenous tissue after 12 days (C) and 25 days (D) from implant (magnification x5). Scale bars= 200 µm; (E-F) H&E images showing scaffold's pores colonization after 12 days (E) and 25 days (F) from implant (magnification x40). Scale bars= 50 µm.

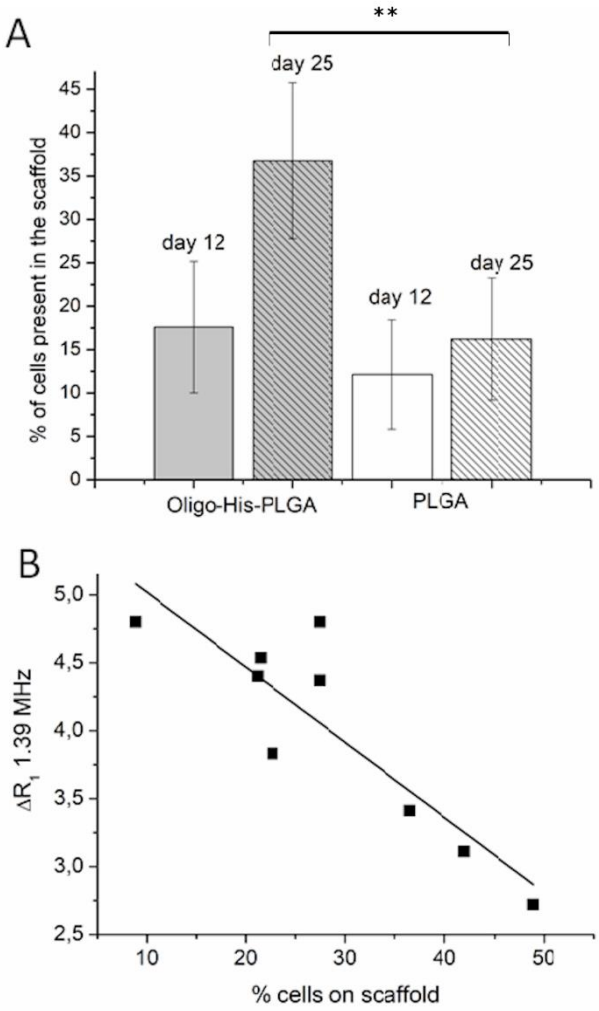

Figure 7. (A) Comparison of cell colonization on oligo-His-PLGA scaffolds (n=9) versus PLGA scaffolds (n=9) after 12 or 25 days from implant (error bars indicate standard deviation, statistical analysis: ** $P < 0.01$, day 12 n=6, day 25 n=6). B) Correlation between the % of cells on the scaffold and the ΔR_1 measured a 1.39 MHz in the NMRD profile by equation 1

Adhesion of tissue cells to biomaterials is an important prerequisite for the successful incorporation of implants or the colonization of scaffolds for tissue engineering [44]. The percentage of haematoxylin positive area was higher in oligo-His-PLGA in comparison to PLGA scaffolds (in particular 25 days after surgical implantation) indicating a higher cell affinity for the oligo-His functionalised biomaterial (**Figure 7A**). Accordingly, it was previously reported that the attachment of fibroblasts depends on the biomaterial surface properties determined by the presence of different functional groups such as amine ($-NH_2$), carboxyl (-COOH), hydroxyl (-OH), methyl ($-CH_3$) and polyethylene glycol (PEG).[45,46]

Faucheux and coworkers[43] demonstrated the significantly higher affinity of murine fibroblasts for surfaces functionalized with $–NH_2$ and –COOH groups with respect to CH_3, PEG and OH. One may surmise that the presence of imidazole groups on the oligo-His-PLGA can have an effect comparable to the one observed for $–NH_2$ groups, endowing the biomaterial with the ability to mimic and/or stimulate cellular functions that promote an improved engraftment ability in respect to the un-functionalised PLGA. The ability to monitor the state of the biomaterial was demonstrated by the observation that the ΔR_1 decrease at 1.39 MHz is linearly and strongly correlated with the percentage of invading cells (Pearson Coefficient r= -0.88, Figure 9B) The lower correlation of ΔR_1 for the peaks centred at 2.03 and 2.73 MHz (r= -0.46. -0.62, respectively, see supplementary **Table S3**) is likely due to the contribution of proteins arising from invading cells, thus confirming the scaffold colonization.

In order to better characterize the typology of cells invading the scaffold a staining for neutrophils and macrophages was performed (**Figure 8**). 12 days after the implant several $CD68^+$ cells were visible at the periphery, while only few neutrophils were detected. After 25 days the number of $CD68^+$ cells and neutrophils remained stable, suggesting the good biocompatibility of the material.

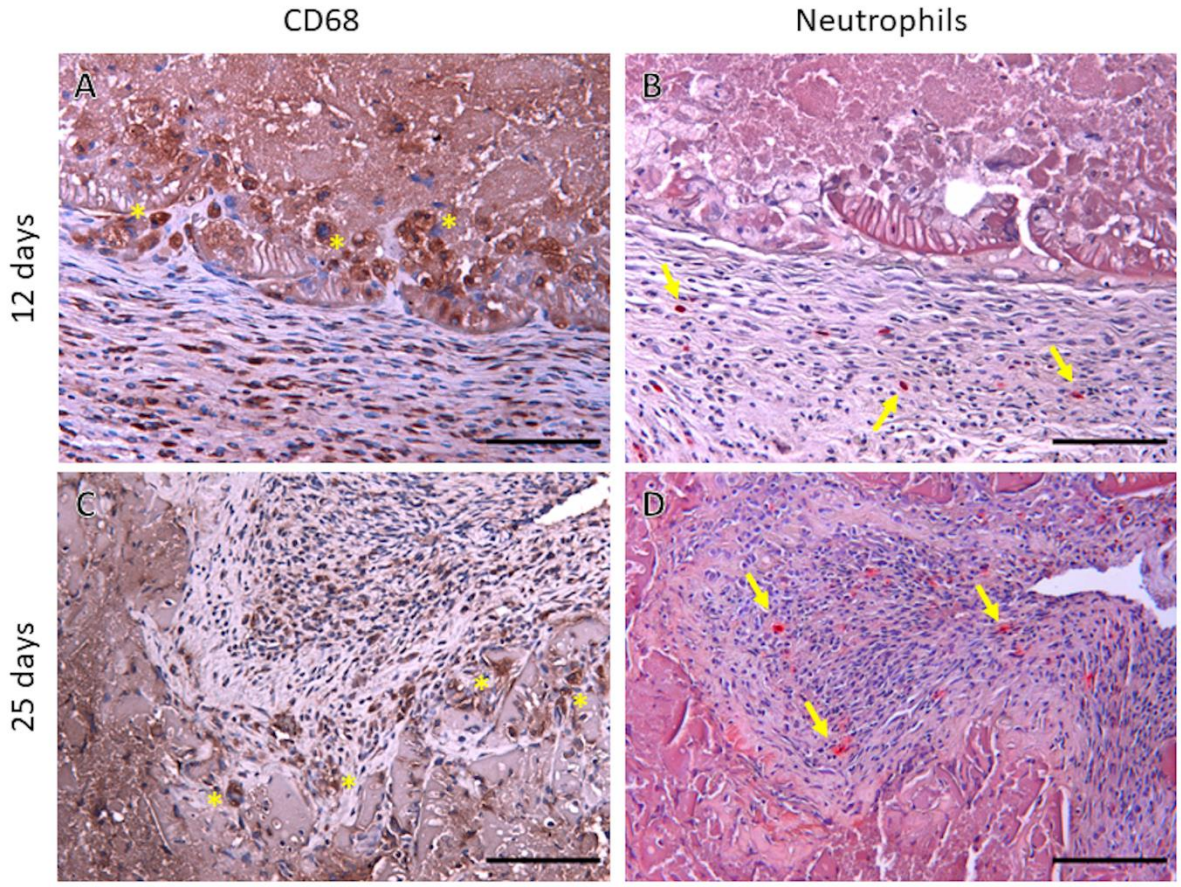

Figure 8. Paraffin sections from oligo-His-PLGA scaffolds were analysed by histology using immunohistochemistry with anti CD68 antibody (A, C) or stained for neuthophil (chloroacetate esterase staining) (B, D). Asterisks indicate engulfing scaffold macrophages. Arrows indicate neuthophils (magnification x20). Scale bars= 100 μm.

4. Conclusion

The herein reported observations show that oligo-His-containing PLGA scaffolds are highly bio-compatible systems for *in vivo* applications. They are progressively colonized by endogenous cells and replaced by the newly formed tissue. The scaffold degradation is obviously well detected in T_{2w} MR images. However further relevant information may be acquired from MRI/NMR of these materials by the observation of the quadrupolar ^{14}N contribution to the water proton relaxation enhancement observed at 1.39 MHz. Importantly, the pH-dependence of the relaxation enhancement response of the imidazole moiety may act as a reporter of the acidification of the microenvironment. Thus the combined information from

T_{2w} images on ordinary MRI scanners coupled to the acquisition of ΔR1 at 1.39 MHz allows getting more inside into the degradation of the scaffold and the pH decrease that accompanies its cellular colonization. [35] More in general the herein reported observations on the frequency-encoded relaxation enhancement paves the way to an innovative concept to generate MRI contrast and highlights the role that FFC-MRI may have, also in the context of the design of exogenous agents that may be considered as potential substitutes of the currently used GBCAs. As herein shown, these reporters may be endowed with responsive properties thus allowing the access to new information from a smart selection of the chemical components of the materials used in medical devices.

Supporting Information
Supporting Information is available

Acknowledgements
This work was performed in the frame of the COST Action AC15209 (EURELAX). The authors acknowledge the Italian Ministry of Research for FOE contribution to the Euro-BioImaging MultiModal Molecular Imaging Italian Node (www.mmmi.unito.it). This project has received funding from the European Union Horizon 2020 research and innovation program under grant agreement No 668119 (project "IDentIFY") and from the ATTRACT project funded by the EC under Grant Agreement No. 777222.

Data availability
All data analysed during this study are included in this published article (and its supplementary information file). Other raw data required to reproduce these findings are available from the corresponding author on reasonable request.

References

[1] K. Dzobo, N.E. Thomford, D.A. Senthebane, H. Shipanga, A. Rowe, C. Dandara, M. Pillay, K.S.C.M. Motaung, Advances in regenerative medicine and tissue engineering: Innovation and transformation of medicine, Stem Cells Int. 2018 (2018). https://doi.org/10.1155/2018/2495848.

[2] K. Ziv, S.S. Gambhir, Bioengineering and regenerative medicine: Keeping track, Nat. Mater. 12 (2013) 180–181. https://doi.org/10.1038/nmat3579.

[3] Z. Pan, J. Ding, Poly(lactide-co-glycolide) porous scaffolds for tissue engineering and regenerative medicine, Interface Focus. 2 (2012) 366–377. https://doi.org/10.1098/rsfs.2011.0123.

[4] S. Pina, J.M. Oliveira, R.L. Reis, Natural-based nanocomposites for bone tissue engineering and regenerative medicine: A review, Adv. Mater. 27 (2015) 1143–1169. https://doi.org/10.1002/adma.201403354.

[5] D.I. Braghirolli, D. Steffens, P. Pranke, Electrospinning for regenerative medicine: A review of the main topics, Drug Discov. Today. 19 (2014) 743–753. https://doi.org/10.1016/j.drudis.2014.03.024.

[6] T.G. Kim, H. Shin, D.W. Lim, Biomimetic scaffolds for tissue engineering, Adv. Funct. Mater. 22 (2012) 2446–2468. https://doi.org/10.1002/adfm.201103083.

[7] F.M. Chen, X. Liu, Advancing biomaterials of human origin for tissue engineering, Prog. Polym. Sci. 53 (2016) 86–168. https://doi.org/10.1016/j.progpolymsci.2015.02.004.

[8] D. Yang, J. Xiao, B. Wang, L. Li, X. Kong, J. Liao, The immune reaction and degradation fate of scaffold in cartilage/bone tissue engineering, Mater. Sci. Eng. C. 104 (2019) 109927. https://doi.org/10.1016/j.msec.2019.109927.

[9] C.Y. Lai, P.J. Wu, S.R. Roffler, S.T. Lee, S.M. Hwang, S.S. Wang, K. Wang, P.C.H. Hsieh, Clearance kinetics of biomaterials affects stem cell retention and therapeutic efficacy, Biomacromolecules. 15 (2014) 564–573. https://doi.org/10.1021/bm401583b.

[10] C.S. Park, T.H. Ha, M. Kim, N. Raja, H. suk Yun, M.J. Sung, O.S. Kwon, H. Yoon, C.S. Lee, Fast and sensitive near-infrared fluorescent probes for ALP detection and 3d printed calcium phosphate scaffold imaging in vivo, Biosens. Bioelectron. 105 (2018) 151–158. https://doi.org/10.1016/j.bios.2018.01.018.

[11] A.K.M. Fleck, U. Kruger, K. Carlson, C. Waltz, S.A. McCallum, X. Lucas Lu, L.Q. Wan, Zonal variation of MRI-measurable parameters classifies cartilage degradation, J.

Biomech. 65 (2017) 176–184. https://doi.org/10.1016/j.jbiomech.2017.10.011.

[12] G. Ferrauto, E. Di Gregorio, W. Dastrù, S. Lanzardo, S. Aime, Gd-loaded-RBCs for the assessment of tumor vascular volume bycontrast-enhanced-MRI, Biomaterials. 58 (2015) 82–92. https://doi.org/10.1016/j.biomaterials.2015.04.026.

[13] L. Biancone, S. Geninatti Crich, V. Cantaluppi, G.M. Romanazzi, S. Russo, E. Scalabrino, G. Esposito, F. Figliolini, S. Beltramo, P. Cavallo Perin, G.P. Segoloni, S. Aime, G. Camussi, Magnetic resonance imaging of gadolinium-labeled pancreatic islets for experimental transplantation, NMR Biomed. 20 (2007) 40–48. https://doi.org/10.1002/nbm.1088.

[14] Q. Li, Z. Feng, H. Song, J. Zhang, A. Dong, D. Kong, W. Wang, P. Huang, 19F magnetic resonance imaging enabled real-time, non-invasive and precise localization and quantification of the degradation rate of hydrogel scaffolds in vivo, Biomater. Sci. 8 (2020) 3301–3309. https://doi.org/10.1039/d0bm00278j.

[15] M.E. Mertens, A. Hermann, A. Bühren, L. Olde-Damink, D. Möckel, F. Gremse, J. Ehling, F. Kiessling, T. Lammers, Iron oxide-labeled collagen scaffolds for non-invasive MR imaging in tissue engineering, Adv. Funct. Mater. 24 (2014) 754–762. https://doi.org/10.1002/adfm.201301275.

[16] S. Hu, Y. Zhou, Y. Zhao, Y. Xu, F. Zhang, N. Gu, J. Ma, M.A. Reynolds, Y. Xia, H.H.K. Xu, Enhanced bone regeneration and visual monitoring via superparamagnetic iron oxide nanoparticle scaffold in rats, J. Tissue Eng. Regen. Med. 12 (2018) e2085–e2098. https://doi.org/10.1002/term.2641.

[17] Y. Liang, A. Bar-Shir, X. Song, A.A. Gilad, P. Walczak, J.W.M. Bulte, Label-free imaging of gelatin-containing hydrogel scaffolds, Biomaterials. 42 (2015) 144–150. https://doi.org/10.1016/j.biomaterials.2014.11.050.

[18] K.W.Y. Chan, G. Liu, X. Song, H. Kim, T. Yu, D.R. Arifin, A.A. Gilad, J. Hanes, P. Walczak, P.C.M. Van Zijl, J.W.M. Bulte, M.T. McMahon, MRI-detectable pH

nanosensors incorporated into hydrogels for in vivo sensing of transplanted-cell viability, Nat. Mater. 12 (2013) 268–275. https://doi.org/10.1038/nmat3525.

[19] R.N. Mariano, D. Alberti, J.C. Cutrin, S.G. Crich, S. Aime, Design of PLGA based nanoparticles for imaging guided applications, Mol. Pharm. 11 (2014) 4100–4106. https://doi.org/10.1021/mp5002747.

[20] V. Raeisdasteh Hokmabad, S. Davaran, A. Ramazani, R. Salehi, Design and fabrication of porous biodegradable scaffolds: a strategy for tissue engineering, J. Biomater. Sci. Polym. Ed. 28 (2017) 1797–1825. https://doi.org/10.1080/09205063.2017.1354674.

[21] L.M. Broche, P.J. Ross, G.R. Davies, M.J. MacLeod, D.J. Lurie, A whole-body Fast Field-Cycling scanner for clinical molecular imaging studies, Sci. Rep. 9 (2019) 10402–10402. https://doi.org/10.1038/s41598-019-46648-0.

[22] D.J. Lurie, S. Aime, S. Baroni, N.A. Booth, L.M. Broche, C.H. Choi, G.R. Davies, S. Ismail, D. Ó hÓgáin, K.J. Pine, Imagerie de resonance magnétique en champ cyclé, Comptes Rendus Phys. 11 (2010) 136–148. https://doi.org/10.1016/j.crhy.2010.06.012.

[23] Rainer Kimmich, Field-cycling NMR Relaxometry: Instrumentation, Model Theories and Applications , R. Soc. Chem. (2018) 358–384. https://doi.org/10.1039/9781788012966.

[24] R.M. Steele, J.-P. Korb, G. Ferrante, S. Bubici, New applications and perspectives of fast field cycling NMR relaxometry., Magn. Reson. Chem. 54 (2016) 502–9. https://doi.org/10.1002/mrc.4220.

[25] S. Baroni, M.R. Ruggiero, V. Bitonto, L.M. Broche, D.J. Lurie, S. Aime, S. Geninatti Crich, In vivo assessment of tumour associated macrophages in murine melanoma obtained by low-field relaxometry in the presence of iron oxide particles, Biomaterials. 236 (2020). https://doi.org/10.1016/j.biomaterials.2020.119805.

[26] M.R. Ruggiero, S. Baroni, S. Pezzana, G. Ferrante, S. Geninatti Crich, S. Aime, Evidence for the Role of Intracellular Water Lifetime as a Tumour Biomarker Obtained

by In Vivo Field-Cycling Relaxometry, Angew. Chemie - Int. Ed. 57 (2018) 7468–7472. https://doi.org/10.1002/anie.201713318.

[27] L.M. Broche, G.P. Ashcroft, D.J. Lurie, Detection of osteoarthritis in knee and hip joints by fast field-cycling NMR, Magn. Reson. Med. 68 (2012) 358–362. https://doi.org/10.1002/mrm.23266.

[28] L.M. Broche, S.R. Ismail, N.A. Booth, D.J. Lurie, Measurement of fibrin concentration by fast field-cycling NMR, Magn. Reson. Med. 67 (2012) 1453–1457. https://doi.org/10.1002/mrm.23117.

[29] D. Kruk, E. Masiewicz, A.M. Borkowska, P. Rochowski, P.H. Fries, L.M. Broche, D.J. Lurie, Dynamics of solid proteins by means of nuclear magnetic resonance relaxometry, Biomolecules. 9 (2019). https://doi.org/10.3390/biom9110652.

[30] B. Halle, Molecular theory of field-dependent proton spin-lattice relaxation in tissue, Magn. Reson. Med. 56 (2006) 60–72. https://doi.org/10.1002/mrm.20919.

[31] E.P. Sunde, B. Halle, Mechanism of 1H-14N cross-relaxation in immobilized proteins, J. Magn. Reson. 203 (2010) 257–273. https://doi.org/10.1016/j.jmr.2010.01.008.

[32] P.H. Fries, E. Belorizky, Simple expressions of the nuclear relaxation rate enhancement due to quadrupole nuclei in slowly tumbling molecules, J. Chem. Phys. 143 (2015) 044202. https://doi.org/10.1063/1.4926827.

[33] E. Di Gregorio, G. Ferrauto, S. Lanzardo, E. Gianolio, S. Aime, Use of FCC-NMRD relaxometry for early detection and characterization of ex-vivo murine breast cancer, Sci. Rep. 9 (2019). https://doi.org/10.1038/s41598-019-41154-9.

[34] S. Geninatti Crich, S. Baroni, R. Stefania, L.M. Broche, N. Senn, D.J. Lurie, J.J. Ross, S. Aime, A novel class of 1H-MRI Contrast Agents based on the relaxation enhancement induced on water protons by 14N imidazole moieties, Angew. Chemie Int. Ed. (2020). https://doi.org/10.1002/anie.202011513.

[35] K. Carter, H.J. Lee, K.S. Na, G.M. Fernandes-Cunha, I.J. Blanco, A. Djalilian, D.

Myung, Characterizing the impact of 2D and 3D culture conditions on the therapeutic effects of human mesenchymal stem cell secretome on corneal wound healing in vitro and ex vivo, Acta Biomater. 99 (2019) 247–257. https://doi.org/10.1016/j.actbio.2019.09.022.

[36] C. Gösweiner, P. Lantto, R. Fischer, C. Sampl, E. Umut, P.O. Westlund, D. Kruk, M. Bödenler, S. Spirk, A. Petrovič, H. Scharfetter, Tuning Nuclear Quadrupole Resonance: A Novel Approach for the Design of Frequency-Selective MRI Contrast Agents, Phys. Rev. X. 8 (2018) 021076. https://doi.org/10.1103/PhysRevX.8.021076.

[37] D. Kruk, E. Umut, E. Masiewicz, C. Sampl, R. Fischer, S. Spirk, C. Goesweiner, H. Scharfetter, 209Bi quadrupole relaxation enhancement in solids as a step towards new contrast mechanisms in magnetic resonance imaging, Phys. Chem. Chem. Phys. 20 (2018) 12710–12718. https://doi.org/10.1039/c8cp00993g.

[38] D. Kruk, E. Masiewicz, E. Umut, A. Petrovic, R. Kargl, H. Scharfetter, Estimation of the magnitude of quadrupole relaxation enhancement in the context of magnetic resonance imaging contrast, J. Chem. Phys. 150 (2019) 184306. https://doi.org/10.1063/1.5082177.

[39] P.J. Ross, L.M. Broche, D.J. Lurie, Rapid field-cycling MRI using fast spin-echo, Magn. Reson. Med. 73 (2015) 1120–1124. https://doi.org/10.1002/mrm.25233.

[40] G. FERRANTE, S. SYKORA, TECHNICAL ASPECTS OF FAST FIELD CYCLING, Adv. Inorg. Chem. 57 (2005) 405–470. https://doi.org/10.1016/S0898-8838(05)57009-0.

[41] M.D. Krebs, K.A. Sutter, A.S.P. Lin, R.E. Guldberg, E. Alsberg, Injectable poly(lactic-co-glycolic) acid scaffolds with in situ pore formation for tissue engineering, Acta Biomater. 5 (2009) 2847–2859. https://doi.org/10.1016/j.actbio.2009.04.035.

[42] Q. Tang, D. Zhao, H. Yang, L. Wang, X. Zhang, A pH-responsive self-healing hydrogel based on multivalent coordination of Ni 2+ with polyhistidine-terminated

PEG and IDA-modified oligochitosan, J. Mater. Chem. B. 7 (2019) 30–42. https://doi.org/10.1039/c8tb02360c.

[43] M.P. McCurdie, L.A. Belfiore, Solid-state complexes of poly(L-histidine) with metal chlorides from the first row of thed-block, J. Polym. Sci. Part B Polym. Phys. 37 (1999) 301–309. https://doi.org/10.1002/(SICI)1099-0488(19990215)37:4<301::AID-POLB4>3.0.CO;2-H.

[42] M. Rahmati, E.A. Silva, J.E. Reseland, C. A Heyward, H.J. Haugen, Biological responses to physicochemical properties of biomaterial surface, Chem. Soc. Rev. 49 (2020) 5178–5224. https://doi.org/10.1039/d0cs00103a.

[43] N. Faucheux, R. Schweiss, K. Lützow, C. Werner, T. Groth, Self-assembled monolayers with different terminating groups as model substrates for cell adhesion studies, Biomaterials. 25 (2004) 2721–2730. https://doi.org/10.1016/j.biomaterials.2003.09.069.

[44] P. Thevenot, W. Hu, L. Tang, Surface chemistry influences implant biocompatibility., Curr. Top. Med. Chem. 8 (2008) 270–80. https://doi.org/10.2174/156802608783790901.